Supplementary Information

Deep metal-assisted chemical etching using a porous monolithic AgAu layer to develop neutral-colored transparent silicon photovoltaics

HyeonOh Shin,†[a,b] Kangmin Lee,†[c] Jinhong Mun,†[a] Deok-Ho Roh,[a,b] Eunhye Hwang,[a,b] Jeonghwan Park,[c] Geunsik Lee,*[a] Kwanyong Seo,*[b,c,d] and Tae-Hyuk Kwon*[a,b,d,e]

[a]Department of Chemistry, School of Natural Science, Ulsan National Institute of Science and Technology (UNIST), Ulsan 44919, Republic of Korea

[b]Center for Wave Energy Materials, UNIST, Ulsan 44919, Republic of Korea

[c]School of Energy and Chemical Engineering, UNIST, Ulsan 44919, Republic of Korea

[d]Graduate School of Carbon Neutrality, UNIST, Ulsan 44919, Republic of Korea

[e]Graduate School of Semiconductor Materials and Device Engineering, UNIST, Ulsan 44919, Republic of Korea

†These authors contribute equally

Experimental explanation

Supplementary Figure and Table

Figure S1. Pattern of the microhole array to fabricate the neutral-colored transparent c-Si.

Figure S2–3. Structure observation of the Ag catalyst according to the amount of ACN added.

Figure S4. Cross-section image of the transparent c-Si via MACE.

Figure S5. C_{dl} calculation of transparent c-Si via MACE.

Figure S6. Contact angle measurement of the Ag precursor on c-Si.

Figure S7. DFT simulation of electroless deposition of Ag.

Transparent c-Si preparation via MACE

The n-type Czochralski Si (100) wafer (200 μm thick, 1–3Ω·cm) was used to fabricate transparent c-Si. Microhole arrays (20% transmittance) were periodically patterned using AZ4330E photoresist (AZ Electronic Materials) via the photolithography process. The patterned c-Si was immersed into the Ag precursor (aqueous 10 mM AgNO$_3$ adding 0–5% AN) for 2 min to deposit the Ag catalyst. MACE was performed by immersing Ag catalyst-deposited c-Si into the etchant (the mixture of 4.8 M HF and 0.44 H$_2$O$_2$) at room temperature until the holes were fully penetrated (ca. 6 h). Microholes were mostly penetrated through MACE, and a few Si nanowires remained were removed by immersing briefly the etched c-Si in ca. 12 M KOH solution, followed by washing immediately with D.I. The photoresist was removed by acetone and the Ag catalyst residue was removed by a diluted nitric acid and an aqua regia.

Electrochemical and structural characterization

Both cyclic and linear sweep voltammetry were performed on a potentiostat/galvanostat/ZRA instrument (Ivium Technologies) using the 3-electrode system. To evaluate the oxidation potential of Ag$^+$, the concentration of 0.1 M was given for the H$_2$SO$_4$ electrolyte to adjust with a similar pH of 4.8 M HF (ca. pH 1.2). Contact angle measurement was performed on Phoenix 300 instrument (SEO). The morphological characterization of the etching catalyst and transparent c-Si was investigated using a field-emission scanning electron microscope (FE-SEM, Hitachi S-4800). The elemental analysis of the etching catalyst was conducted by energy dispersive x-ray spectroscopy in high-resolution transmission electron microscopy (HR-TEM, JEM-2100F).

Computational simulation of the electroless deposition of Ag

Spin-polarized density functional theory calculations were performed by using the Vienna ab-initio simulation package (VASP) code.[1] The plane-wave energy cutoff 400 eV was adopted with PBE parameterization of GGA exchange-correlation functional.[2] We constructed a 9-layered slab for a dihydride Si (100) surface with a 2×2 cubic unit cell whose lattice constant is 5.43 Å, and we inserted a sufficient vacuum region greater than 20 Å to minimize unphysical interaction between periodic images. All structures were optimized in 1×1×1 k-mesh by fixing the bottom 5 layers for each slab until all the atomic forces are less than 0.01 eV/ Å with the van der Waals correction by Grimme's D3 scheme.[3]

Galvanic replacement by Au

The Ag catalyst deposited silicon substrate was immersed in the 1 mM $KAuCl_4$ in 6 M HF solution for ca. 1 min. and washed immediately using distilled water. The catalyst color turned from gray to dark yellow because a thin Au layer formed on the porous monolithic Ag layer. Ag^+ concentration in etchant was calibrated and measured by ICP-MS (Figure S13). Patterned c-Si (20% transmittance) with dimensions of 1×1 cm^2 was immersed in 10 mL of the etchant, following which MACE was performed for 6 h.

c-Si TPV fabrication

A p-n junction and back-surface field (BSF) were formed on the transparent c-Si by the spin-on-dopant method. Before the doping process, a 2 µm-thick SiO_2 layer was selectively formed on the sidewall of the microholes as a diffusion barrier via plasma-enhanced chemical deposition (PECVD). After the formation of the SiO_2 diffusion barrier, doping processes were conducted. Initially, the phosphorus dopant source (P509, Filmtronics) was spin coated onto a dummy Si wafer at a spin coating speed of 2000 rpm. The wafer was then baked on a hot plate at 200°C for 20 minutes to eliminate the organic solvent. The rear side of the transparent c-Si wafer was indirectly placed facing the P509-coated dummy wafer using by Si spacers (thickness $\approx$ 500 µm), to form a BSF. A diffusion doping process was subsequently carried out in a tube furnace, under a mixed gas atmosphere of N_2 (500 sccm) and O_2 (125 sccm) at 880°C. Following the formation of the BSF, the phosphorous silicate glass and SiO_2 diffusion barrier on the substrate were eliminated using buffered oxide etchant (BOE). Subsequently, a SiO_2 diffusion barrier was redeposited on the rear side of the transparent c-Si wafer through PECVD. An emitter layer was then formed on it using a boron dopant source (B155, Filmtronics). The boron dopant source was spin coated onto a dummy Si wafer at a spin coating speed of 2000 rpm, followed by baking at 200°C for 20 minutes. The front side of the transparent c-Si wafer was indirectly positioned facing the B155-coated dummy wafer, using by Si spacers (thickness $\approx$ 500 µm). A diffusion doping process was subsequently performed in a tube furnace under a N_2 atmosphere (500 sccm) at 880°C. After the doping process, SiO_2 diffusion barriers were removed using BOE. After forming the p-n junction and BSF, a 10-nm-thick Al_2O_3 layer was deposited through the atomic layer deposition (ALD) process to minimize surface recombination. In addition, to reduce the surface reflection, a 70-nm-thick SiNx layer was formed on the front surface of the device using PECVD. As the front electrode, a microgrid

electrode, which has a high transmittance of over 95%, was then applied.[4-6] As the rear electrode, 700-nm-thick silver (Ag) was deposited by thermal evaporation (See Figure S15).

Photovoltaic characterization

The minority carrier lifetime and the implied V_{oc} were determined using the quasi-steady-state photoconductance method (WCT-120, Sinton Instruments). The optical transmittance was determined using a UV-visible near-infrared spectrophotometer (Cary 5000, Agilent) equipped with a 110-mm integrating sphere. The photovoltaic properties were investigated using a solar simulator (Class AAA, Oriel Sol3A, Newport) under AM 1.5G illumination. The EQE spectra were measured using a Xe light source and a monochromator in the wavelength range of 300–1,100 nm.
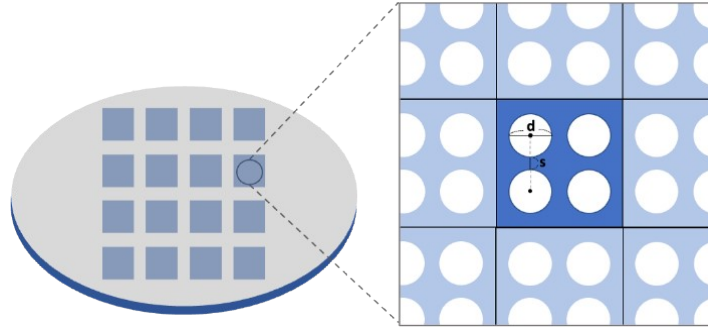
Figure S1. Schematics of the pattern of the microhole array to fabricate the neutral-colored transparent c-Si.

This pattering was designed to transmit visible light without diffraction and by considering the minimum angle of resolution for humans to ensure that the individual microhole-shaped-transmission windows are not recognized by the human eye. Microholes are arranged based on their number (n), diameter (d), and spacing (s) to consider the filling fraction of c-Si. In this study, we aimed for a filling fraction of 80% (i.e., 20% transmittance) as a representative and the corresponding parameters are in Table S1 below.

Table S1. Diameter and spacing of microholes (Transmittance = 20%).

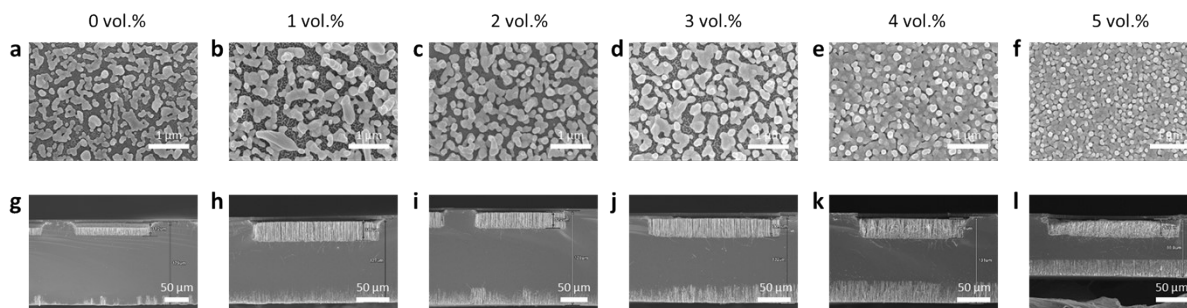| # of microhole (n)	Diameter (d, µm)	Spacing (s, µm)
625	100	100

Figure S2. (a–f) Structure variation of the Ag catalyst via electroless deposition according to the amount ACN added in the Ag precursor. The shape altered gradually from the particles to the porous monolithic layer by the increasing amount of ACN. (g–l) Cross-section of the chemically etched hole (1 h) in c-Si based on the corresponding formed-Ag catalyst, measured by SEM. The etching rate was retained well up to 4 vol.% ACN condition because the porous structure of the Ag catalyst accommodates the etchant diffusion during MACE.
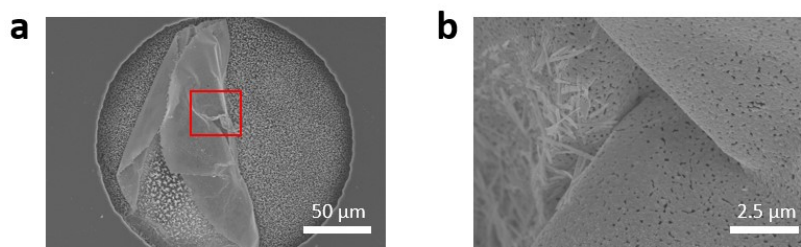

Figure S3. SEM image of the porous monolithic Ag layer that peels off. (a) The high networking between each Ag particle was observed owing to the function of ACN and (b) the enlarged image at the red square region of Figure S3a also shows evenly distributed pores in its whole layer.
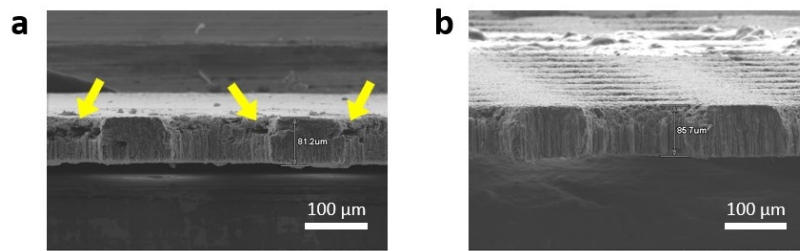
Figure S4. Cross-section image of the transparent c-Si via MACE based on (a) the particle-form (0 vol.% ACN) and (b) porous monolithic layer of Ag (4 vol.% ACN). The lateral etching on the sidewall (yellow arrows) was observed for Ag particles due to its random movement but this tendency was suppressed with the porous monolithic Ag layer owing to its cooperative motion.

In this experiment, the c-Si backside was exposed because we focused to evaluate the degree of defect generation according to the catalyst characteristics. Backside etching would occur by the parasite Ag that originates from the dissolution and re-nucleation process of Ag. But we protected the backside of the Si wafer using a photoresist (AZ4330E) when we fabricated the c-Si TPV to prevent any adverse etching.
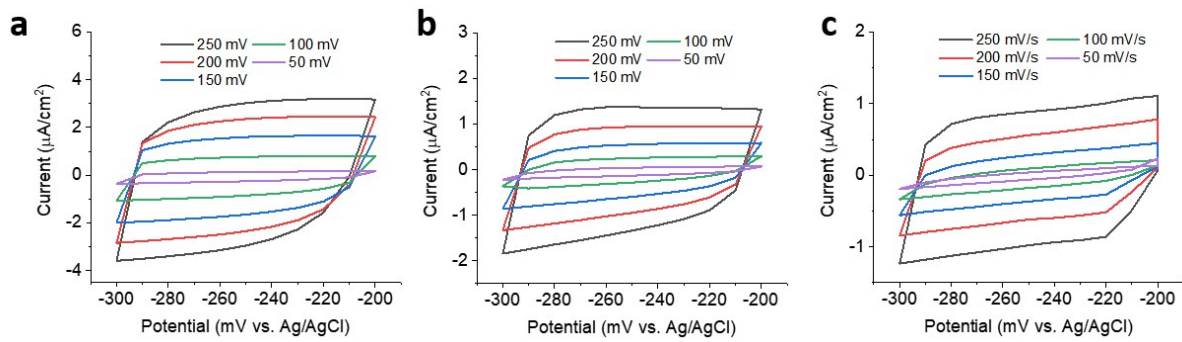
Figure S5. Cyclic voltammetry measurement of transparent c-Si via MACE using (a) the Ag particles, (b) porous monolithic Ag, and (c) AgAu layer. The 3-electrode system was prepared which consists of transparent c-Si (working electrode), Ag/AgCl (reference electrode), 0.5 M H_2SO_4 (electrolyte), and Pt wire (counter electrode) to obtain the cyclic voltammetry curve in the range of the non-faradaic region (−0.3 to −0.2 V vs Ag/AgCl).

The surface area of each transparent c-Si was approximated electrochemically from their double-layer capacitance (C_{dl}) which is expressed shown in the equation followed:[7]

$$C_{dl} = \frac{i_c}{v}$$

where i_c is the charging current ($\frac{J_{anodic} - J_{cathodic}}{2}$) at middle potential and v is the scan rate. The plot of i_c as a function of v yields a straight line with a slope equal to C_{dl}.
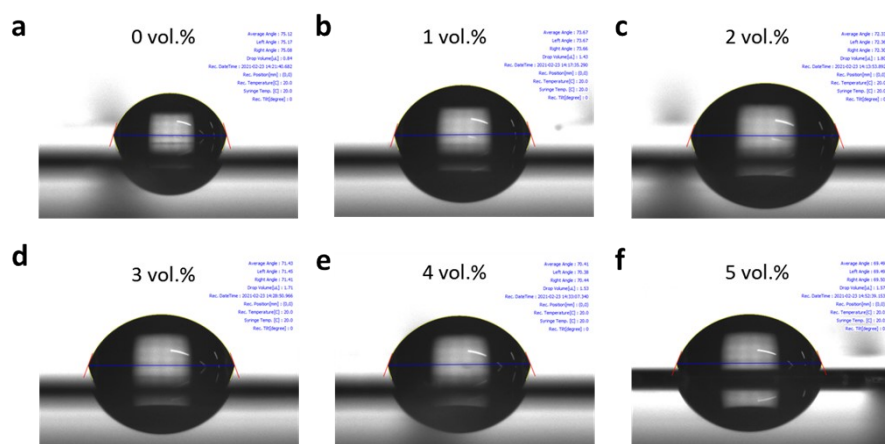
Figure S6. Contact angle measurement of aqueous 10 mM AgNO$_3$ solution on c-Si. 0–5 vol.% of ACN was added to the Ag precursor to confirm the function of ACN as the surfactant, and detection was carried out right after dropping the Ag precursor. The wettability of the precursor increases gradually as the ACN amount increases, which implies a better interaction between the Ag precursor and the c-Si surface.
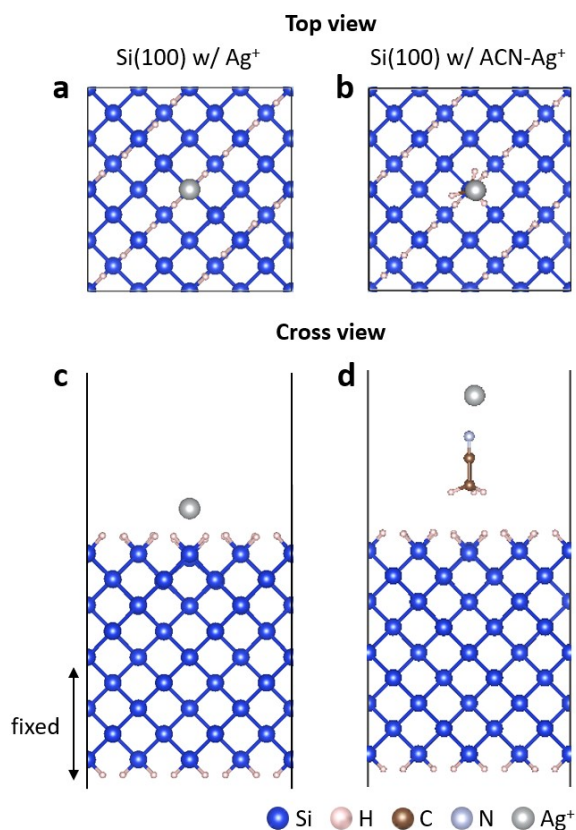
Figure S7. Density functional theory-based theoretical (DFT) simulation of the interaction between Ag ion and dihydride Si (100) in the absence (a,c) and presence (b,d) of ACN.

We calculated the binding energy of Ag^+ or $ACN\text{-}Ag^+$ on the dihydride Si (100) surface by the equation as follows:

$$E_b = E_{clean\text{-}ads} - (E_{clean} + E_{ads})$$

where E_b is binding energy, $E_{clean\text{-}ads}$ is substrate energy with absorbate, E_{clean} is substrate energy without absorbate, and E_{ads} is adsorbate energy. In Ag^+ calculation, we constructed cells with different lengths and extrapolated their energy to get appropriate binding energy without unphysical interactions in the periodic boundary condition.

In presence of ACN, Ag^+ coordinates on the nitrile function of ACN and its assembly absorbate on the dihydride Si (100) surface based on the methyl group of ACN, leading Ag^+ toward the dihydride Si (100) surface effectively.
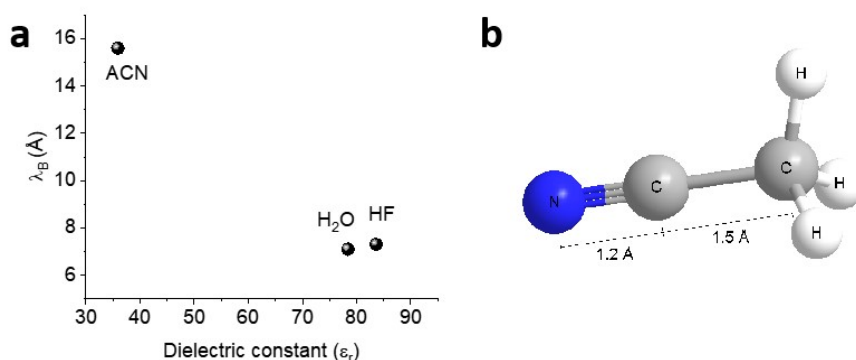
Figure S8. (a) Bjerrum length depending on each environment and (b) the approximated length of ACN.

Electroless deposition of Ag occurs spontaneously by the electron transfer from the Si valence band. In this study, ACN intercepts between Ag^+ and c-Si substrate to improve the interaction, forming the porous monolith Ag layer. As for the distance between them, there is the addition of ACN length (over 2.7 Å, Figure S8b), which might disturb the reduction of Ag^+. To address this issue, we calculated the Bjerrum length which is the distance to separate the charges (electron and hole) bonded electrostatically under the given temperature and it is assumed to be the equation below:[8]

$$\lambda_B = \frac{e^2}{4\pi\varepsilon_0\varepsilon_r k_B T}$$

where λ_B is Bjerrum length, e is the elementary charge (1.60×10^{-19} C), ε_0 is the vacuum permittivity (8.85×10^{-12} F/m), ε_r is the relative dielectric constant, k_B is the Boltzmann constant (1.38×10^{-23} J K^{-1}), T is the absolute temperature. It should be noted that ε_r of ACN (35.9) and H_2O (78.4) are under 298 K while ε_r of HF (84.0) is under 273 K.[9, 10]

As shown in Figure S8a, the longer λ_B was derived for ACN (15.6 Å) compared to HF (7.0 Å) and H_2O (7.1 Å). In other words, the vicinity of the c-Si surface (i.e., ACN-rich environment) is favorable to reduce Ag^+ despite the additional length of ACN, accelerating the Ag nucleation.
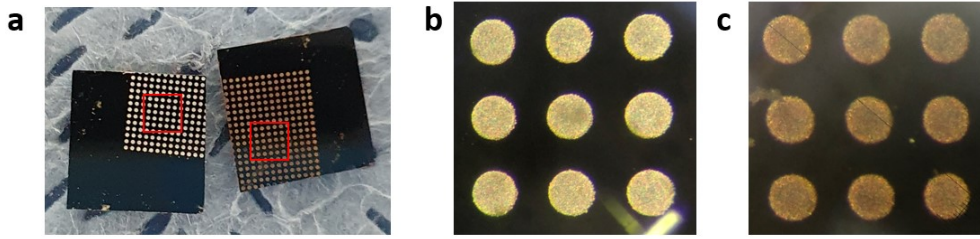
Figure S9. (a) Photograph of the photoresist-patterned c-Si after deposition of the porous monolith Ag (left) and AgAu (right) layer. (b and c) Enlarged images of the corresponding red square region of Figure S9a. It was optically observed that the color of the porous monolith Ag layer was changed to deep yellow after galvanic replacement (GR) due to the Au element being its outer surface.
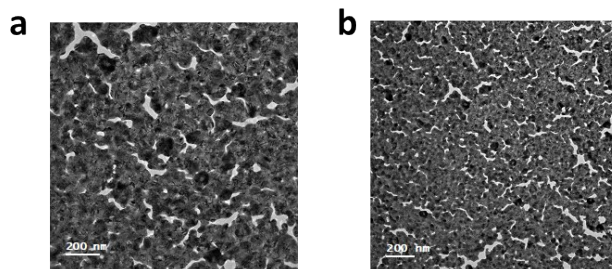

Figure S10. HR-TEM image of the porous monolithic Ag layer (a) before and (b) after processing GR with Au. The porous monolithic structure retained well, demonstrating no structure deformation after GR.

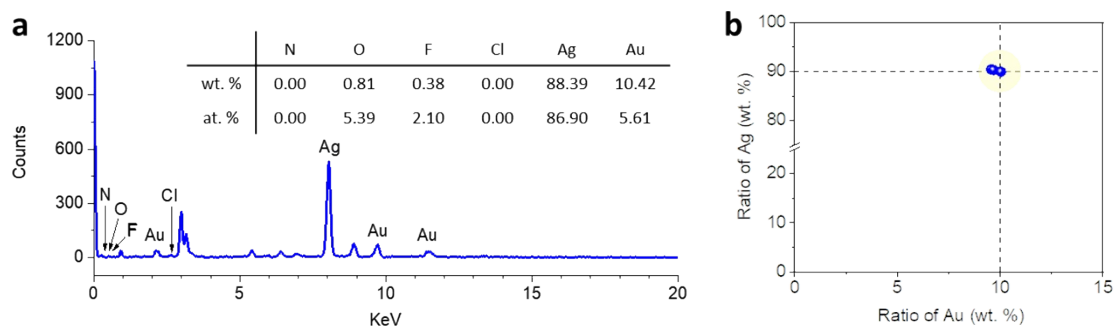|	N	O	F	Cl	Ag	Au
wt. %	0.00	0.81	0.38	0.00	88.39	10.42
at. %	0.00	5.39	2.10	0.00	86.90	5.61

Figure S11. (a) EDX spectrum of the porous monolith AgAu layer. ca. 10 wt.% of Au was detected because the outer surface of the porous monolith Ag layer was encapsulated with Au element during GR. It is noteworthy that no Cl element was observed after GR using 1 mM $KAuCl_4$, which means AgCl hardly formed on the porous monolith AgAu layer, thus maintaining its etching activity. (b) Weight percentages of Ag and Au in the four porous monolithic AgAu layers.
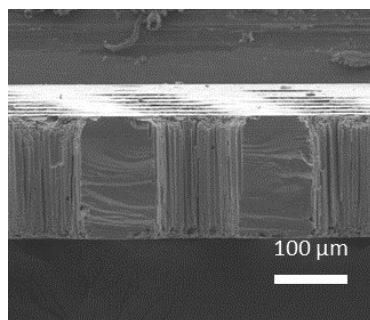
Figure S12. Cross-section SEM image of transparent c-Si via MACE based on the porous monolith AgAu layer. A smoother surface was observed compared to that of the monometallic (Ag) catalyst (Figure S4) because the Au element enables the etching catalyst to improve the chemical stability during MACE, resulting in the high quality of transparent c-Si.
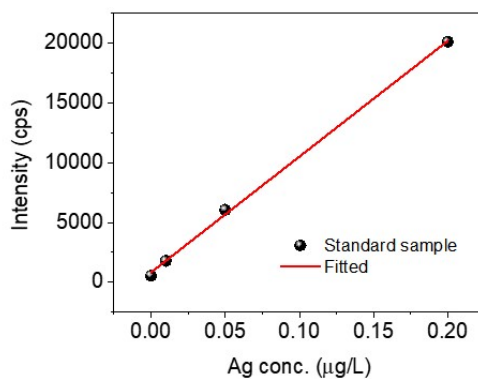

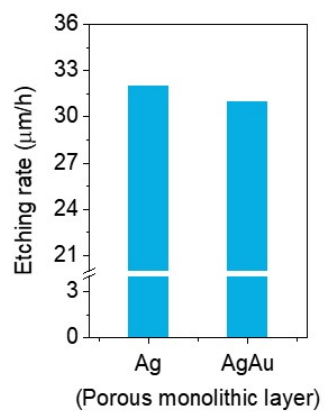Figure S13. Calibration curve of Ag ions as obtained via ICP-MS.

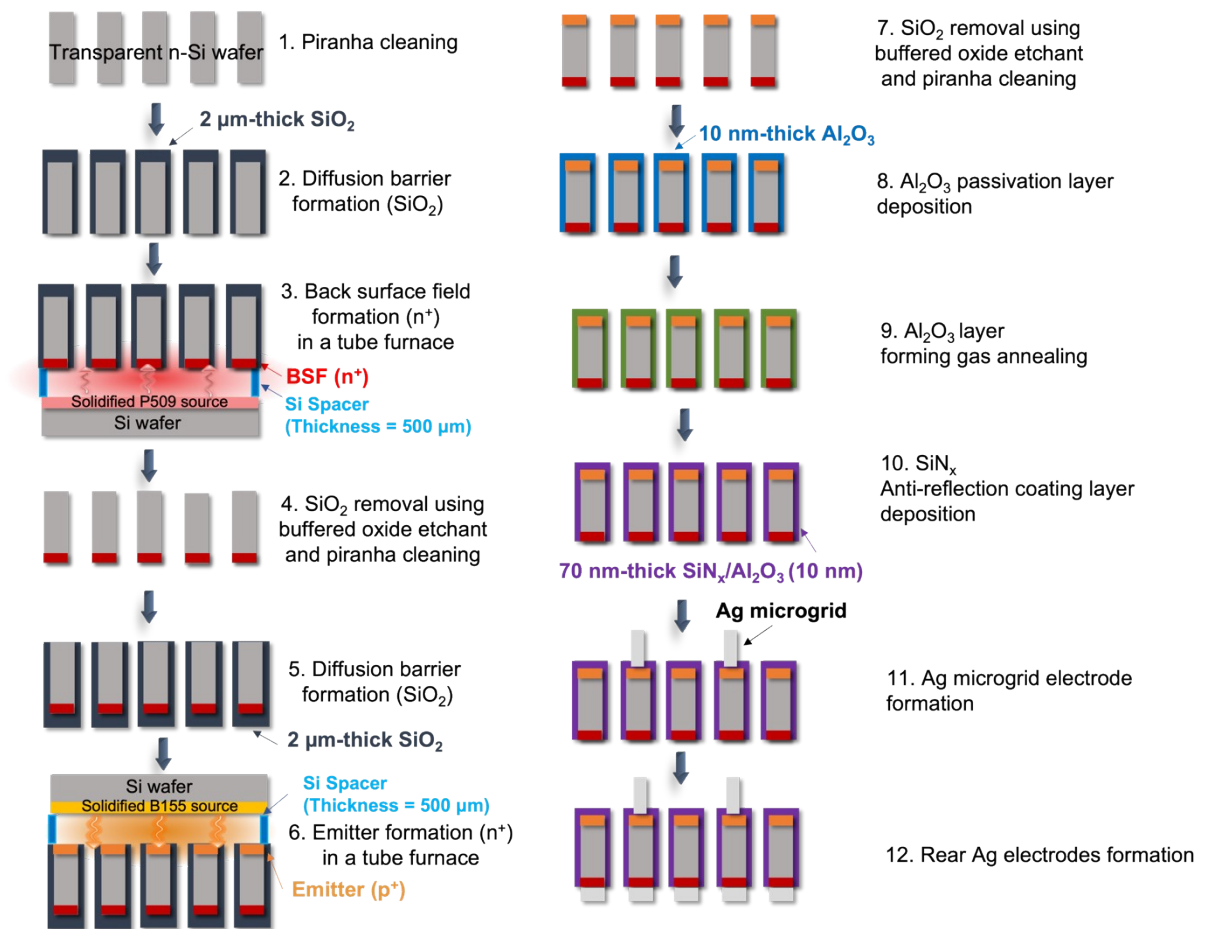Figure S14. Etching rate depending on the absence/presence of Au in the etching catalyst.

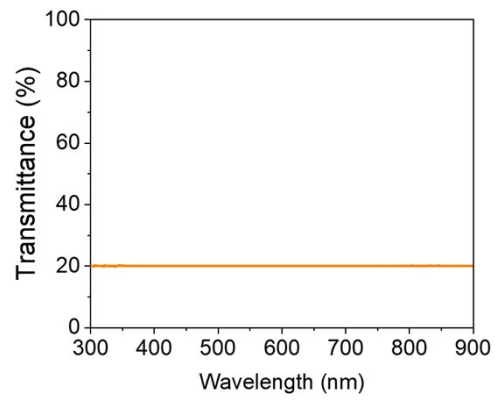Figure S15. A detailed description of the fabrication of the c-Si TPV.

Figure S16. Transmittance measurement of c-Si TPV via MACE based on the porous monolith AgAu layer.
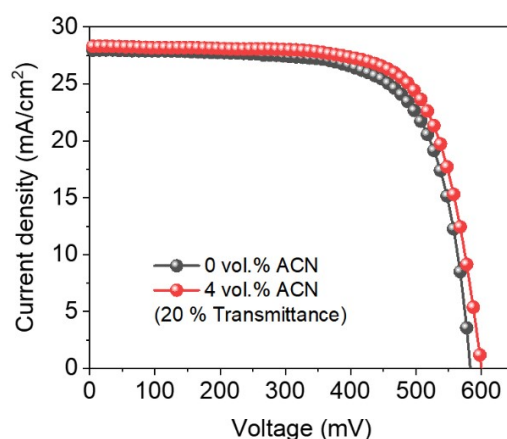
Figure S17. Current density-voltage characteristics of MACE-processed c-Si TPV according to the structure of Ag catalyst under AM 1.5 G spectral conditions at 25°C. Open circuit voltage is improved for 4 vol.% ACN condition, arising from less defect generation on transparent c-Si owing to the cooperative motion of the porous monolith Ag layer (4 vol.% ACN).

Table S2. Performance parameter of MACE-processed c-Si TPV according to the structural characteristic of Ag catalyst.

The Ag catalyst	J_{sc} (mA cm^{-2})	V_{oc} (mV)	FF (%)	PCE (%)
0 vol.% ACN (Ag Particles)	28	588	72.4	11.9
4 vol.% ACN (Porous monolithic Ag layer)	28.3	597	73.3	12.4

J_{sc} is short circuit current, V_{oc} is open-circuit voltage, FF is fill factor, and PCE is power conversion efficiency. This measurement was performed under AM 1.5 G, 25°C condition. It is noted that the best performances were recorded on this table.
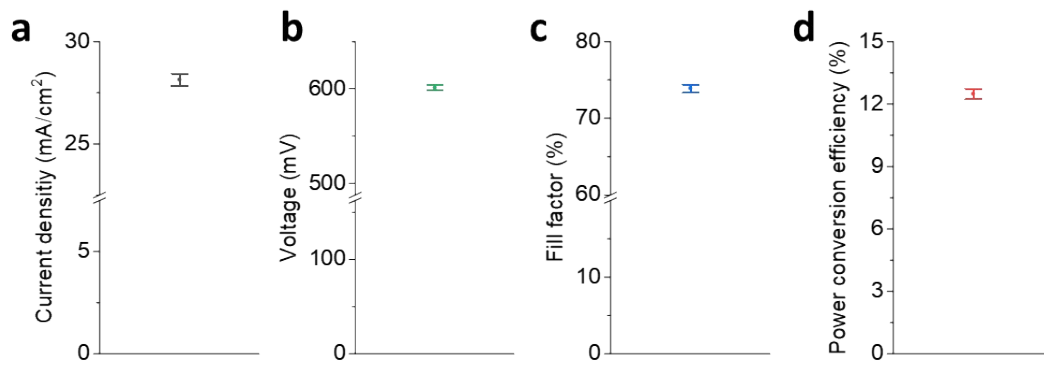
Figure S18. Statistical distribution of the performance of c-Si TPV, including (c) J_{sc}, (d) V_{oc}, (e) FF, and (f) PCE.

Table S3. Performance parameters of the c-Si TPV.

Devices	J_{sc} (mA/cm^2)	V_{oc} (mV)	FF (%)	PCE (%)
1	28.7	602	74.1	12.8
2	28.5	608	75.1	13.0
3	28.1	598	73.2	12.3
4	27.8	603	73.5	12.3
5	28.0	601	74.0	12.5
6	28.2	602	74.5	12.6
7	28.3	599	73.4	12.4
8	27.6	598	73.6	12.1
Average	28.2	601	73.9	12.5
Standard deviation	0.4	3.3	0.6	0.3

Table S4. Minority carrier lifetimes of the transparent c-Si depending on the fabrication methods and fabrication step.

	Before doping	After doping	After Al$_2$O$_3$ passivation
Planar	89.2 μs	40.5 μs	690.2 μs
Transparent c-Si (DRIE)	7.6 μs	2.9 μs	61.1 μs
Transparent c-Si (MACE-A)	16.3 μs	6.1 μs	133.5 μs

REFERENCE

1. G. Kresse and J. Furthmüller, *Comput. Mater. Sci.*, 1996, **6**, 15-50.
2. J. P. Perdew, K. Burke and M. Ernzerhof, *Phys. Rev. Lett.*, 1996, **77**, 3865-3868.
3. T. Bučko, S. Lebègue, J. Hafner and J. G. Ángyán, *Phys. Rev. B*, 2013, **87**, 064110.
4. H.-D. Um, I. Hwang, N. Kim, Y. J. Yu, M. Wober, K.-H. Kim and K. Seo, *Adv. Mater. Interfaces*, 2015, **2**, 1500347.
5. K. Lee, N. Kim, K. Kim, H.-D. Um, W. Jin, D. Choi, J. Park, K. J. Park, S. Lee and K. Seo, *Joule*, 2020, **4**, 235-246.
6. J. Park, K. Lee and K. Seo, *Cell Rep. Phys. Sci.*, 2022, **3**, 100715.
7. C. C. McCrory, S. Jung, I. M. Ferrer, S. M. Chatman, J. C. Peters and T. F. Jaramillo, *J. Am. Chem. Soc.*, 2015, **137**, 4347-4357.
8. S. N. Hood and I. Kassal, *J. Phys. Chem. Lett.*, 2016, **7**, 4495-4500.
9. A. A. Maryott and E. R. Smith, *Table of Dielectric Constants of Pure Liquids*, U.S. Government Printing Office, 1951.
10. L. G. Gagliardi, C. B. Castells, C. Ràfols, M. Rosés and E. Bosch, *J. Chem. Eng. Data*, 2007, **52**, 1103-1107.